Arabian Journal of Chemistry 16 (2023) 105307

Contents lists available at ScienceDirect

Arabian Journal of Chemistry

journal homepage: www.sciencedirect.com

Original article

Fishbone derived-hydroxyapatite supported Ni-Zr nanocatalyst for CO_2 methanation: Synergistic effects of support and zirconia

Ngoc Doan Trang Tran [a,b,1], Thi Ngoc Han Che [a,b], Thi Thuy Van Nguyen [c,d], Ba Long Do [a,b,c,1], Thanh Gia-Thien Ho [c], Phung Anh Nguyen [c], Thi Thuy Phuong Pham [c,d], Nguyen Tri [c,d,*], Huynh Ky Phuong Ha [a,b,*]

[a] University of Technology – VNU-HCM, 268 Ly Thuong Kiet Str., HCM City, Vietnam
[b] Vietnam National University Ho Chi Minh City, Thu Duc District, Ho Chi Minh City, Vietnam
[c] Institute of Chemical Technology – VAST, 01A TL29 Str., District 12, HCM City, Vietnam
[d] Graduate University of Science and Technology– VAST, 18 Hoang Quoc Viet Street, Cau Giay District, Hanoi, Vietnam

ARTICLE INFO

Article history:
Received 21 June 2023
Accepted 21 September 2023
Available online 26 September 2023

Keywords:
CO_2 methanation
Hydroxyapatite
Fishbone
Zirconia
Nickel nanocatalyst

ABSTRACT

Herein, the effectiveness of nickel-zirconia nanocatalyst decorated on hydroxyapatite (HA) is examined as a potential candidate for the methanation of carbon dioxide (CO_2). Co-impregnation was used to produce undoped nickel as well as zirconia-doped nickel catalysts that were supported on hydroxyapatite derived from fishbone. The prepared catalysts were characterized using several methods. With the molar ratio of H_2/CO_2 fixed at 4/1, the catalytic activity was evaluated through the CO_2 methanation at low temperatures ranging of 250–––400 °C. A high dispersion of nickel particles over the catalyst surface with a size range of 30–––40 nm was provided as a function of HA and zirconia. This led to an improvement in the reducibility and CO_2 adsorption capacity of the catalysts and an enhancement of the efficiency in CO_2 methanation. At a reaction temperature of 400 °C, the data reveal that the 10Ni/HA sample doped with 4 wt% zirconia was the most effective. At this temperature, the CO_2 conversion reached 92.9%, and the CH_4 selectivity reached approximately 100%.

1. Introduction

In the period 2015–––2040, the global energy demand is expected to increase by about 30% compared to the present time (Zhao et al., 2022), and to date, the main supply of energy still comes from fossil fuels. These natural resources need millions of years to form; however, the increasing demand of humanity is leading to the gradual exhaustion of this fuel. Besides, obtaining energy through burning fossil fuels also releases greenhouse gases, leading to global warming (Wai et al., 2021). In addition, the fossil fuel extraction also poses many threats to the environment, affecting vegetation and topsoil, increasing soil erosion, and losing habitat for many species. Under climate change and environmental pollution pressure, energy transition and carbon emission reduction is an inevitable orientation that deserves utmost attention. To meet the goal of declining the CO_2 concentration in the second half of this century as the commitment to the "Net-Zero global CO_2 emission" (Jiang et al., 2022); CO_2 conversion technology is the center of interest. Besides the recent development of photocatalytic CO_2 reduction which may adapt to the upcoming issues (Jiang et al., 2022; Muiruri et al., 2022), the conventional thermal CO_2 methanation (Sabatier reaction) also seems appealing to investigators. Especially, when this reaction is a part of the "Power to Gas" technology, where hydrogen is achieved from water electrolysis splitting, and the optional excess hydrogen can be transformed into CH_4 for storage via the Sabatier reaction. Then, the generated methane is stored or used for many different purposes (Mebrahtu et al., 2019). The advantages of the innovation in hydrogen production (electrolysis and other technologies (Ye et al., 2023), as well as renewable

* Corresponding authors.
E-mail addresses: ntri@ict.vast.vn (N. Tri), hkpha@hcmut.edu.vn (H. Ky Phuong Ha).
[1] Those authors contributed equally.
Peer review under responsibility of King Saud University.

Production and hosting by Elsevier

https://doi.org/10.1016/j.arabjc.2023.105307
1878-5352/

energy, are creating pathway for the CO_2 methanation and the PtG process to be able to be applied in the future energy grid.

The process of CO_2 methanation is an exothermic reaction, mainly occurring in the temperature range of 200–––400 °C, and in the reaction process, depending on different influencing factors, by-products such as carbon, CO, etc, can be produced. Besides tuning the reaction conditions, the catalysts also play an important role to obtain the efficient transforming CO_2 into CH_4. Many catalysts based on precious metals (Rd, Rh, Ru, Ir, etc) and transition metals (Ni, Co, Fe, Mn) with various supports (SiO_2, Al_2O_3, TiO_2, and SiO_2-Al_2O_3) and medium pore materials have been studied to improve the efficiency of converting CO_2 into methane gas (Lee et al., 2021; Komatsu and Furukawa, 2015; Namvar et al., 2023; Bakar et al., 2015). Due to the low cost and accessibility, Ni-metal-based catalysts are considered to be the most common, exhibiting high activity, good selectivity. The morphology, crystal lattice phase, size, dispersion and supporting interactions of the Ni catalyst, which can be tuned by altering the support, have a significant influence on the CO_2 methanation (Kuznecova and Gusca, 2017; Van et al., 2020). Applying and studying the support are common orientations to improve the catalysts' performance.

On the other hand, converting by-products or waste in agriculture or industry into applicable materials is a helpful strategy in the concept of sustainable development. One of the materials being studied and applied as support nowadays is hydroxyapatite (HA). HA has the molecular formula $Ca_{10}(PO_4)_6(OH)_2$, exists in crystalline form, hexagonal structure in different shapes depending on the synthesis method or other conditions in the synthesis process. The HA crystals are interconnected, creating gaps and porosity for the material. This material can be synthesized from organic materials such as animal bones, corals, seashells, eggshells, fish scales, shrimp shells, etc., or chemical methods using starting materials such as compounds containing calcium and phosphorus. Though HA originated from natural or chemical sources have the same nature and chemical composition, synthesizing from industrial by-products or waste has a more positive response to the environment. The FAO (Food and Agricultural Organization) estimates that only about 50–––60% of fish caught is for human consumption, the rest consists of by-products such as bones, skin, and offal. It is considered a very low value by-product. Today, this by-product is used in animal feed production; however, a large amount of the remaining waste is wasted and discharged directly into the environment, causing a great impact on the environment. Therefore, taking advantage of wasted by-products to synthesize new materials brings economic benefits and contributes to solving environmental problems.

With the thermal stable property, the application of HA as support for Ni-based catalyst has been conducted in our previous study in the CO_2 methanation reaction. In order to increase the activity of the Ni/HA catalyst, it's recommended to add a second metal (M) such as Fe, Zr, Co, La, Mg, or Ru to form an alloy system Ni–M or metal oxide to improve reducing properties, enhance mobility, improve metal dispersion and prevent metal sintering (Su et al., 2016). Among those promoters, ZrO_2 is widely used due to its outstanding properties of enhanced activity, high thermal stability, and low carbon deposition rate due to its large number of active electron sites on the surface, base sites (OH groups, O^{2-} adsorbed), acid-base pairs Zr^{4+}–O^{2-} and oxygen vacancies. ZrO_2s interactions with metals and other oxides can affect CO_2 adsorption and activation, enhance H_2 dissociation and atomic hydrogen diffusion, and change the reaction and binding pathways of the intermediate to react to further conversion (Li and Chen, 2019). This rare earth oxide has been studied on some Ni-based catalysts system, however, the addition and effect of this promoter on the Ni/HA catalyst haven't been elucidated yet. Hence, in this work, the interaction of ZrO_2 with Ni active sites and the HA support is explored in the thermal catalytic CO_2 methanation.

2. Experimental

2.1. Fabrication of catalyst

The raw salmon bone was collected from seafood manufacturers in Vietnam. All the chemicals used in the experiment were purchased from Merck and used without further purification. The preparation of HA was taken place as described in our previous research (Tri et al., 2020). 1.0 g of the dried salmon bone was introduced to 50 mL of distilled water, then 14 mL H_3PO_4 1 wt% was added dropwise into the above mixture. The mixture was adjusted to pH = 10 by NH_4OH 5 wt% solution and stirred vigorously for 2 h. After stirring, the mixture was transferred into Teflon-line autoclave and heated to 120 °C for 7 h. The precipitate after the hydrolysis was isolated by centrifuging, washed with distilled water and ethanol, then dried at 80 °C for 12 h. The HA support was obtained after calcining the dry precipitate in the air at 800 °C for 1 h.

Ni-ZrO_2/HA was prepared by the impregnation method. Calculated amounts of $Ni(NO_3)_2{\cdot}6H_2O$, $ZrOCl_2{\cdot}8H_2O$, and HA support were mixed with a decent amount of distilled water. After mixing, the mixture was dried at 3 levels of temperature (80, 100, and 120 °C) for 2 h for each temperature. The calcination was carried out at 600 °C for 4 h (a heating rate of 10 °C/min) to obtain the NiO-ZrO_2/HA. Before the catalytic activity evaluation, a pretreatment of NiO-ZrO_2/HA in a pure H_2 flow (3 L/h) was taken place and the Ni-ZrO_2/HA catalyst was officially obtained. The Ni content was fixed at 10 wt%. The catalysts were assigned 10NixZr/HA, in which × value is the wt.% of ZrO_2 and × = 2, 4, and 6.

2.2. Characterization

The physical–chemical characteristics of the obtained samples were studied by several methods (Van et al., 2020), including X-ray diffraction on a Bruker D2 Phaser Xray diffractometer with Cu Kα radiation and recorded in 2θ = 10 – 80° with a step size of 0.03°; EDS spectrum on a JEOL JST-IT 200 instrument; ultraviolet–visible diffuse reflectance spectroscopy (UV–Vis DRS) on a V-770 UV–visible/NIR spectrophotometer; nitrogen adsorption – desorption isotherms at – 197 °C on a Nova 2200e instrument with the sample pretreated in a 1.8 L/h N_2 flow at 300 °C for 2 h; field-emission scanning electron microscopy on Hitachi S4800 instrument; high-resolution transmission electron microscopy (HR-TEM) on JEOL JEM 1400 instrument; hydrogen temperature-programmed reduction (H_2-TPR) carried out on a microreactor in a gas mixture of 10% H_2/N_2 at a flow rate of 1.8 L/h using a gas chromatograph GOW-MAC 69–––350 with a TCD detector and the used sample of 50 mg; and CO_2-programmed temperature desorption (CO_2-TPD) also carried out on a microreactor in He at a flow rate of 1.8 L/h from 50 to 800 °C at a ramping rate of 10 °C/min with 100 mg of catalyst adopted in a quartz reactor and reduced at 450 °C for 1 h in pure H_2 at a flow rate of 1.8 L/h prior to being cooled down to 50 °C.

2.3. Catalytic activity

For catalytic activity testing, a quartz tube placed in a furnace was used as the reactor system. The catalyst bed is a mixture of 0.5 g quartz and 0.5 g catalyst in the same size of 0.25–––0.50 m m. The reduction process was carried out under a 3 L/h H_2 flow at 400 °C for 2 h with a heating rate of 10 °C/min. After the pretreatment, the catalytic activity of all samples was tested at the

temperature range of 250–––400 °C with a total flow rate of 6 L/h consisting of a $CO_2/H_2/N_2$ ratio of 3/12/85 mol%. To determine the CO_2 conversion and CH_4 selectivity in product flow, the reaction mixture was analyzed on a gas chromatograph (Agilent 5890 Series II) using a thermal conductivity detector with a capillary column (TG-BON Q, 30 m length, 12 μm inter diameter, 0.32 μm thickness) and a flame ionization detector with a capillary column (DB624, 30 m length, 0.32 mm outer diameter, 0.25 μm thickness). The gas mixtures of CH_4 6 mol.% in N_2 and CO 6 mol.% in N_2 were used as a reference to monitor CH_4 and CO produced in the output. CO_2 conversion (X_{CO_2}) and CH_4 selectivity (S_{CH_4}) were calculated according to Eq. (1) and Eq.(2):

$$X_{CO_2} = \frac{F^{in}_{CO_2} - F^{out}_{CO_2}}{F^{in}_{CO_2}} \quad (1)$$

$$S_{CH_4} = \frac{F^{out}_{CH_4}}{X_{CO_2}.F^{in}_{CO_2}} \quad (2)$$

where $F^{in}_{CO_2}$ is the input molar of CO_2; $F^{out}_{CO_2}$ is the remaining molar of CO_2; and F_{CH_4} is the molar of produced CH_4.

3. Results and discussions

3.1. Physico-chemical characteristics

The XRD patterns of catalysts with different Zr contents (Fig. 1a) shows that the presence of HA hexagonal phase in all samples is indicated by the diffraction peaks at 2θ = 10.9, 16.9, 21.6, 22.8, 26.1, 27.8, 28.7, 31.8, 32.0, 32.9, 34.0, 39.9, 46.8, 49.5, 50.5, 51.3, 52.0, 53.0, 60.2, 61.7, 64.0, 65.1, and 77.0° (JCPDS card No.09–432). Besides, the β-TCP $Ca_3(PO_4)_2$ phase with low concentration was also detected with low intensive diffraction peaks at 2θ = 13.7, 31.2, 34.7, 35.6, 37.6, 57.1, 58.0, and 78.3° (JCPDS card No.09–169). The presence of β-TCP $Ca_3(PO_4)_2$ relates to pH and sintering temperature (Le et al., 2012; Boukha et al., 2019). The same phenomenon was also observed in Taimai's study (Tamai et al., 2007), in which a ratio of Ca/P < 1.67 induced the decomposition of HA, resulting in the formation of β-TCP $Ca_3(PO_4)_2$. The characteristic diffraction peaks of Ni appear at 2θ = 44.7, 51.9, and 76.8° (JCPDS No.04–0850). According to Standard Card mp-20194, the characteristic peaks for ZrO_2 appear at 2θ = 24.3, 29.7, 33.7, 34.8, 42.1, 49.3, 50,1, 57.9, 59.3, 61.7, 70.9, and 73.5°. However, these ZrO_2 peaks are hardly observed. This phenomenon could account for the relatively low content of ZrO_2, or maybe some of the Ni's peaks have coincided with the HA peaks (2θ = 33.7, 49.3, 50.1, and 61.7°). The texture properties of HA support and undoped nickel as well as zirconia-doped nickel catalysts are given in the Table 1. The addition of zirconia to the 10Ni/HA catalyst shows the effect of decreasing the Ni crystalline size (15.3 nm down to 5.5 nm), which agrees with several pieces of literature investigating the impact of ZrO_2 promoter in the Ni-based catalysts (Roh et al., 2004; Cai et al., 2011; Chong et al., 2019). The improved dispersal of active sites could result in the amelioration of the catalyst's overall activity. The Ni crystalline size calculated by the Debye-Scherrer equation is 5.5 nm for the reduced 10Ni4Zr/HA sample, three times smaller than that of the pure 10Ni/HA sample.

The H_2-TPR results (Fig. 1b and Table 1) were obtained to assess the reducibility of the supported Ni species (Boukha et al., 2022). Fig. 1b illustrates that the H_2-TPR results of zirconia-doped catalysts exhibit typical peaks corresponding to the same temperature areas as the profiles of unmodified catalysts. The 10Ni/HA sample's TPR profile exhibited four reduction peaks below 450 °C, which can respectively be classified as 4 types of NiO species (α, **β**$_1$, β$_2$, and γ). The first characteristic is ascribed to the reduction of surface oxygen species (α species), which induces the oxygen vacancies on the catalyst's surface. The second and third reduction peaks can be attributed to the reduction of NiO that exhibits a weak and medium interaction with HA (β species), which further classified into β_1 and β_2 (Boukha et al., 2019). The last reduction peak at higher temperature, which assigned to the γ- NiO species, might be induced from the bulk NiO particles that strongly attached to the HA support surface. Intriguingly, the addition of Zr alters the peaks toward lower temperatures, demonstrating the promoter effect of zirconium on the reduction of Ni species. More specifically, the reduction temperatures of these catalysts are lower than those of the unmodified catalysts, suggesting improved metal phase dispersion since ZrO_2 minimizes the weakening of the NiO–support contact and enhances the capacity to scatter NiO on the HA surface (Boukha et al., 2022). In addition, the Fig. 1b demonstrates that the zirconia-doped catalysts exhibit faint reduction signals at 600 °C; these reduction signals pertain to the reduction process of the NiO–ZrO_2 interaction phases or surface ZrO_2 in the doped catalysts. The ZrO_2 doping level is modest (2–6 wt%); hence the decrease signal is not strong. Furthermore, regardless of the Zr-modified sample, the amounts of consumed H_2 are considerably greater than those required for the reduction of a stoichiometric NiO phase. The observed tendency can be attributed to the presence of highly reducible Ni sites, most likely those located close to the NiO-ZrO_2 interface. This is consistent with the observed increase in the density of defective metallic Ni crystallites with increasing Zr loading, as demonstrated by XRD data for reduced samples. Notably, our results show that Zr promotes the reducibility of 10NixZr/HA catalysts.

To evaluate the CO_2 adsorption capacity of the ZrO_2 modified catalyst for the methanation process, the CO_2-TPD desorption method was performed and the results are shown in Fig. 1c. All catalysts show a wide and high intensity CO_2 desorption region in the temperature range of 80–––300 °C, indicating that the catalyst surface contains a large number of medium and weak base centers. Low CO_2 desorption peaks at temperatures from 500 °C onwards, especially at above 700 °C are possibly accounted for strong base sites. It was found that CO_2 adsorbed on medium-intensity basic sites could be readily desorbed from the catalyst surface (Pan et al., 2014) to promote CO_2 methanation. From Table 1, the CO_2 desorption capacity of the 10NixZr/HA catalysts is higher than that of the 10Ni/HA catalyst. This could be associated to the more uniform Ni nanoparticles dispersing on the ZrO_2-HA surface. According to researches (Diallo-Garcia et al., 2014; Mihet and Lazar, 2018), CO_2 is primarily adsorbed on surface hydroxyl groups and metal nanoparticles affect CO_2 adsorption capacity. The addition of ZrO_2 also provided new active sites that could absorb CO_2, since ZrO_2 is a quantitative oxide and the hydroxyl provided by it can also increase the number of reactive sites and enhance CO_2 adsorption. ZrO_2 can inhibit carbon deposition and Ni sintering due to its strong oxygen storage capacity (Yang et al., 2020). The enhanced Ni dispersion and the slight decrease of primary sites could suggest a more harmonious more harmony combined adsorption of H_2 and CO_2, proposing a better catalytic activity in the hydrogenation of CO_2 to methane.

The hydrogen consumption (in H_2-TPR analysis) and CO_2 desorption capacity (in CO_2-TPD analysis) are illustrated in Fig. 1d. As being mentioned above, the addition of ZrO_2 promotes the reduction of NiO species, corresponding to the increased amount of consumed hydrogen in H_2-TPR analysis. Although the strong metal-support interaction can enhance the catalytic stability through preventing the Ni sites from agglomerating, weakening those interactions by adding ZrO_2 may also improve the catalytic activity with more presenting Ni metal sites. The maximum hydrogen consumption is observed in the 10Ni4Zr/HA's profile, indicating more ZrO_2 loading might cover Ni sites and slightly decreases

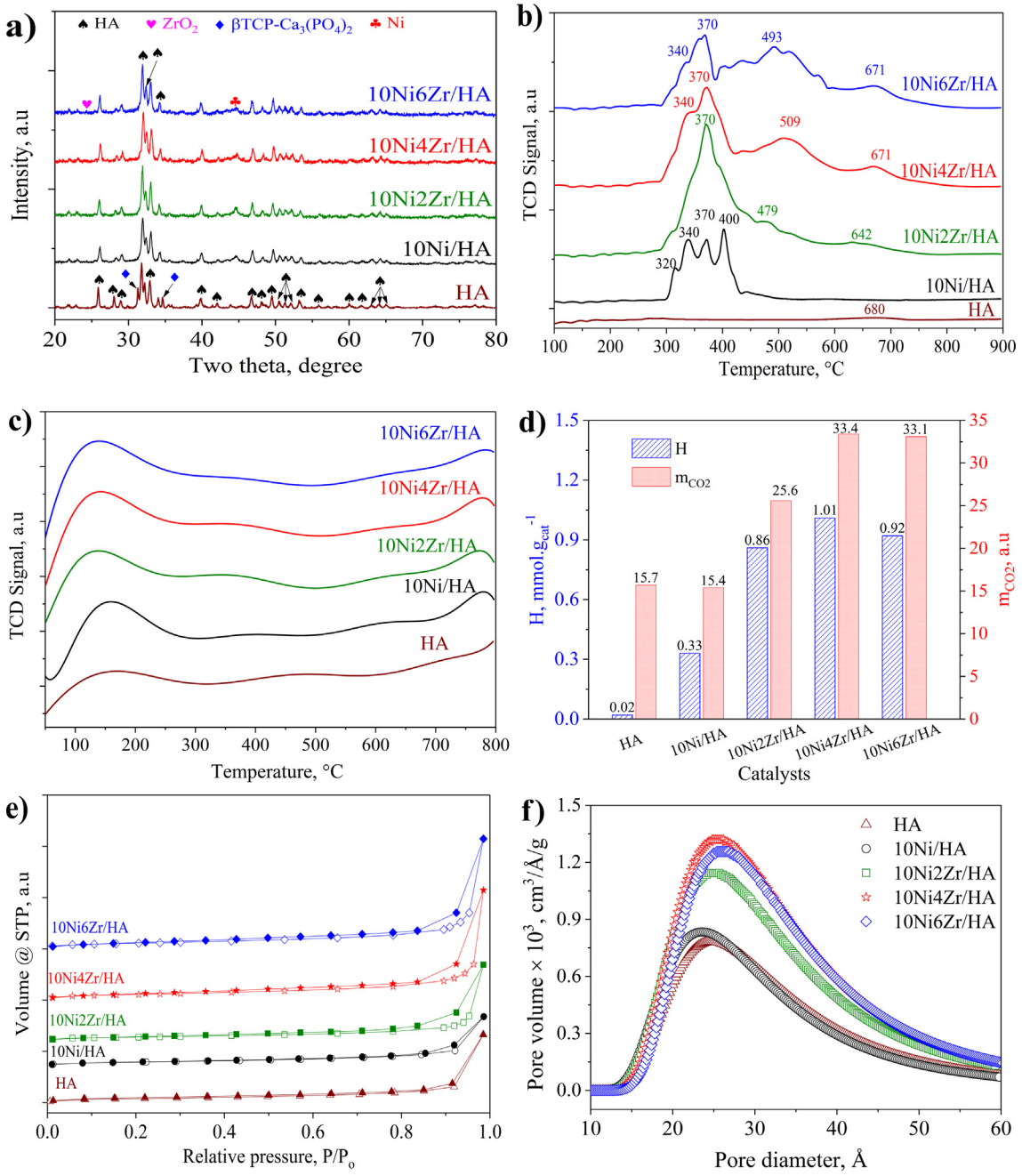

Fig. 1. XRD patterns (a), H_2-TPR (b) and CO_2-TPD (c) profiles, the hydrogen consumption (H) from H_2-TPR results and the desorbed CO_2 amount ($(m_{CO_2})m_{CO_2}$) from CO_2-TPD results (d), N_2 adsorption/desorption isotherms (e), BJH pore diameter distribution (f), and and of 10NixZr/HA catalysts.

the Ni site density on the surface. The dispersion of Ni onto the HA surface didn't alter the basic property of the catalyst, implied by the approximately same CO_2 desorption capacity as seen in Fig. 1d. Adding ZrO_2 produces more CO_2 adsorption sites, and the CO_2 adsorption capacity reaches its peak in the 4 wt% ZrO_2 modification. The excess ZrO_2 (higher than 4 wt%) does not induce more basic sites.

Fig. 1e indicates that the isotherm N_2 adsorption–desorption diagrams of all the examined samples are of type III with hysteresis loops corresponding to the H3 class of the IUPAC classification (Li et al., 2023). The presence of a medium pore structure, as indicated by isotherms of type III, is advantageous for CO_2 adsorption as well as the transport of reactants and intermediates during the reaction (Wang et al., 2019). The absence of capillary condensation in the isotherms of the catalyst sample at low pressures indicates that HA does not have a porous capillary structure (El Shafei et al., 2004). Fig. 1f reveals that the pore size distribution for all samples ranges between 10–––60 Å, which is typical for materials with medium pore sizes. The 10Ni4Zr/HA catalyst has a maximum mean pore diameter of 26 Å, with a slightly higher pore volume compared to other analyzed samples. This textural property is suitable for use for application in catalytic CO_2 methanation (the kinetic diameters of CO_2 and H_2 correspond to 0.33 nm and 0.29 nm) (Li et al., 2006). The specific surface area of the modified catalyst is moderately more considerable than that of the unmodified one, which could be induced by the smaller nanoparticles, having a larger area/volume ratio compared to their bulk material.

The FESEM images (Fig. 2) show that all catalysts have rough and porous surfaces, and the particles have a spherical shape. Two particle sizes were observed on the catalyst surface: large

Table 1
The texture properties of samples.

Samples	d_{HA}[a], nm	d_{Ni}[a], nm	S_{BET}[b], $m^2.g^{-1}$	d_{pore}[b], nm	V_{pore}[b], $cm^3.g^{-1}$	T_{max}[c], °C
HA	8.7	–	13.8	2.48	0.018	680
10Ni/HA	8.7	15.3	15.6	2.36	0.019	320, 340, 370, 400
10Ni2Zr/HA	8.7	9.2	17.3	2.45	0.023	370, 479, 642
10Ni4Zr/HA	8.7	5.5	19.7	2.56	0.032	340, 370, 509, 671
10Ni6Zr/HA	8.7	5.5	18.9	2.50	0.028	340, 370, 493, 671

[a] *Average crystal sizes of HA at 2θ = 26.1° (d_{HA}) and Ni at 2θ = 44.7° (d_{Ni}) estimated by Scherrer equation;*
[b] *BET surface (S_{BET}), average pore diameter (d_{pore}), pore volume (V_{pore}) of catalysts from BET adsorption isotherm analysis;*
[c] *The maximal temperature of reduction peaks (T_{max}) from H_2-TPR results.*

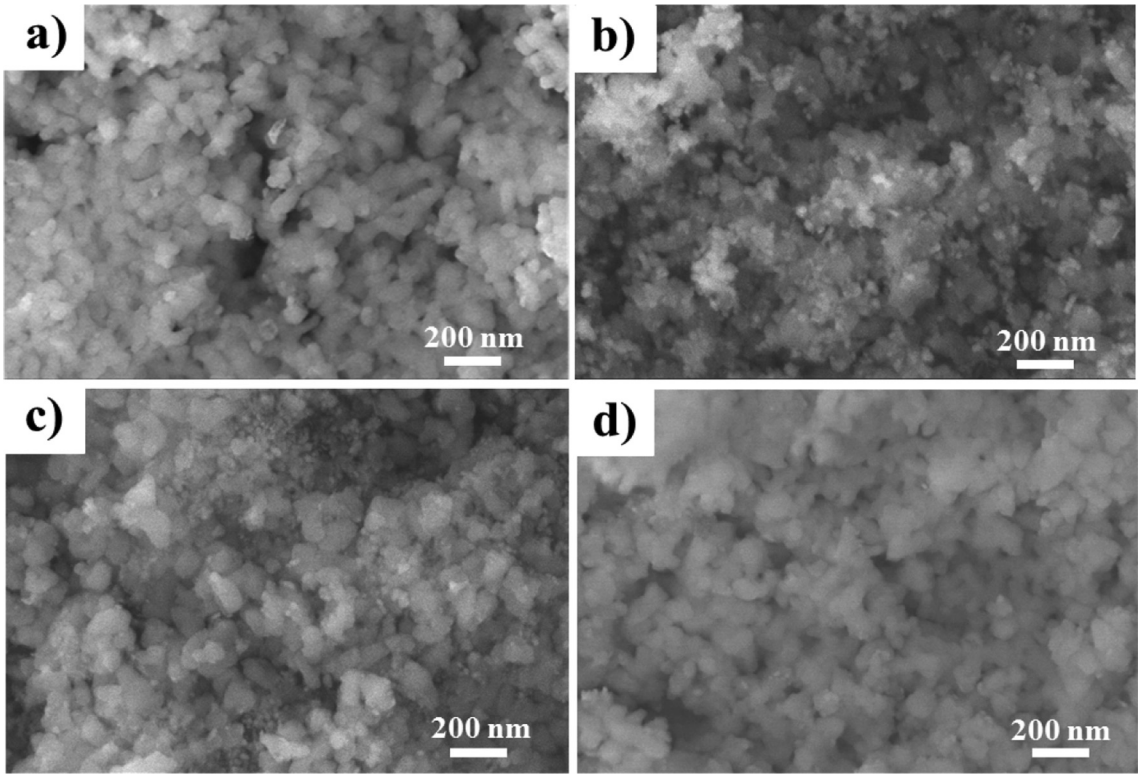

Fig. 2. SEM images of samples; a) 10Ni/HA, b) 10Ni2Zr/HA, c) 10Ni4Zr/HA, and d) 10Ni6Zr/HA.

HA particles and smaller particles of the active metal phase. The unmodified catalyst has a surface of highly concentrated and dense nanoparticles, stacked on top of each other, explaining why this catalyst has the lowest specific surface area (Fig. 2a). Meanwhile, on the surface of ZrO_2 modified Ni/HA catalysts (Fig. 2b-d), it is observed that small spherical particles, with a size of approximate 10 nm, are sparsely distributed and relatively more evenly spread. The FESEM result is consistent with the increase in specific surface area of the modified catalyst compared with the unmodified one in BET result.

The SAED and HR-TEM results (Fig. 3a-c) show the microstructural properties of the 10Ni4Zr/HA sample. The SAED image (Fig. 3a) shows that the nanoparticles are uniformly crystalline with several observed diffraction rings of HA (d = 0.34 and 0.28 nm assigned to (002) and (211) planes), and Ni (d = 0.20 and 0.17 nm associated to (111) and (200) plane). In addition, a faded ring with a respective d-spacing of 0.24 nm could be attributed to the (111) plane of NiO, indicating a part of the catalyst is not reduced into Ni^0. The HRTEM images (Fig. 3b and c) show that the nanoparticles exist with a size range of 30–––40 nm, which is consistent with the captured SEM images and the crystal size calculated from the XRD result. The particles tend to clump together. The HRTEM image also shows bright patches corresponding to ZrO_2 and Ni centers corresponding to dark patches. ZrO_2 particles tend to agglomerate to form large masses with capillary pores and Ni evenly distributed on the surface and in the developed pores.

Based on the EDS results (Fig. 3d), it was found that the mass composition of the elements on the catalyst surface is relatively close to the theoretical calculation, which are O (35.81%), P (15.93%), Ca (34.26%), Ni (10%), and Zr (4%). Slight deviations between experimental and theoretical values exist, possibly due to the impregnation method, since adequate contact cannot be guaranteed in all cases between the metal salt solution and the support during sample drying (Daza et al., 2009). The Ca/P molar ratio < 1.67 agrees with the appeared diffraction peaks of β-TCP $Ca_3(PO_4)_2$ analyzed in the XRD spectrum. Moreover, the colourful dots on the EDS mapping results (Fig. 3e) demonstrated the uni-

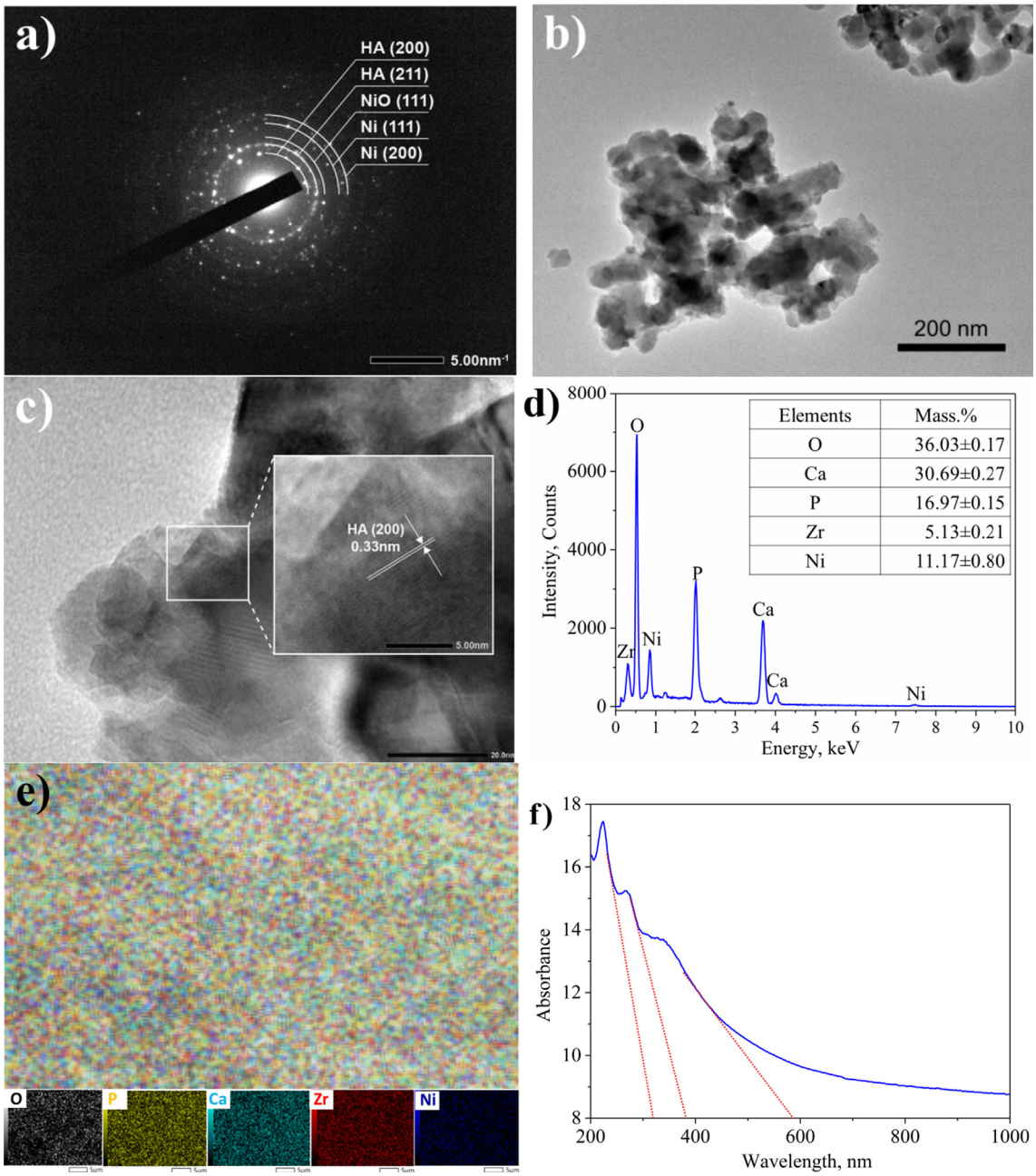

Fig. 3. SAED (a), HRTEM (b and c) images, EDS spectrum and component (d) and mapping (e) of elements, and the UV–Vis DRS spectrum (f) of 10Ni4Zr/HA sample.

form distribution of components on the material surface and the high dispersion of Ni on the support. The UV–Vis analysis results of the typical catalyst, 10Ni4Zr/HA (Fig. 3f), reveal three distinct absorbance regions. The first region lies within the wavelength range of 320 nm, characteristic of ZrO_2 absorption (Soni et al., 2022). The second region falls within the wavelength range of 380 nm, indicative of Ni or NiO absorption (Srihasam et al., 2020). Finally, the third region is observed at a wavelength of 585 nm, representing HA absorption (Pal et al., 2020). Based on these findings, it can be deduced that the material 10Ni4Zr/HA has been successfully synthesized.

3.2. Activity of catalysts

The catalytic CO_2 conversion of catalysts is given in Fig. 4a as temperature functions. Under the same reaction condition, in the temperature range of 250–––400 °C, the CO_2 conversion of the ZrO_2-modified catalyst samples was significantly higher than that of the unmodified catalyst sample. At low temperature, the CO_2 conversion increased slowly, but from about 300 °C, the CO_2 conversion increased rapidly and reached a maximum value at 400 °C for all modified samples. ZrO_2 is a weak hydrophilic (Li and Chen, 2019), beneficial for water desorption and thermodynamically promoting CH_4 formation. ZrO_2 plays many roles in different catalysts, a reasonable load of ZrO_2 can enhance the active metal's dispersion, reducing the crystal size of the catalyst, enlarging the surface area and increasing the Ni^0 active site (from H_2-TPR result), improving H_2 adsorption and CO_2 conversion.

The effect of ZrO_2 can be explained by the mechanism by which ZrO_2 adsorbs CO_2, while Ni adsorbs and dissociates H_2. The adsorbed CO_2 will interact with bridging OH groups on the surface of ZrO_2 to form bicarbonate, an essential intermediate for methane

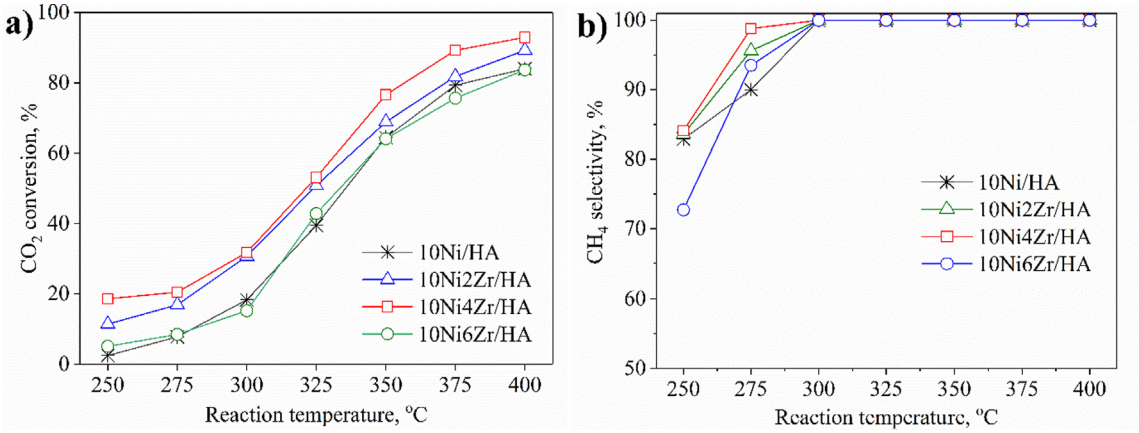

Fig. 4. CO_2 conversion (a) and CH_4 selectivity (b) of 10NixZr/HA catalysts in CO_2 methanation.

synthesis. The role of ZrO_2 is also involved in creating vacancy oxygen sites. This enhancement is due to many oxygen vacancies on the surface of m-ZrO_2, which enhances the adsorption capacity. t-ZrO_2 with abundant emptiness also affects the catalytic performance (Li and Chen, 2019).

As shown in SEM images, the compactness of the catalyst particles in NiZr/HA samples was less than that of Ni/HA. It is demonstrated that zirconia can limit agglomeration on the support, promoting Ni particles' dispersion and stabilization. Combined with the results of BET and XRD, 10Ni4Zr/HA has a specific surface area of 19.7 m^2/g and the best Ni dispersion on the HA support, which could be one of the main reasons for the highest catalytic activity. At 400 °C, the catalyst achieved 92.9% CO_2 conversion, 8.3% higher than the unmodified one. However, when the denaturation content increased from 4 to 6 wt%, the CO_2 conversion decreased, although the ZrO_2 addition reduced the crystal size. This could be due to decreases in the Ni^0 active site (calculated by the hydrogen consumption (H) in Fig. 1d) as well as the dispersion of catalyst shown in the SEM images (Fig. 2) when increasing the ZrO_2 content up to 6 wt%, suggesting that the ZrO_2 content has an optimal range in affecting the catalyst performance. When the ZrO_2 content exceeds the required value, the activity of the catalyst decreases due to the influence of the specific surface area of the catalyst, the dispersion of Ni decreases, or the size of NiO crystals increases too much higher than the value desired. In the case of the catalyst containing higher ZrO_2 content, the lower amount of Ni can prevent the conversion of CO_2 to CO via RWGS, and the right amount of ZrO_2 will benefit methane formation. This fact proved that 10Ni4Zr/HA is one of the catalysts having high activity for CO_2 methanation.

The enhanced interaction between Ni and Zr not only promotes the overflow of H spilling from Ni to the support, which is beneficial for CO_2 hydrogenation and intermediates but also alleviates the clogging of the pore structure by restricting the average size of the Ni particles on the used catalysts to a size smaller than the average pore size. In addition, the increasing Ni particle size improved the low-temperature CO_2 conversion by enhancing the CO_2 adsorption of the catalysts to OCO*. The addition of Zr inhibited carbon deposition by reducing the number of active metal sites and increasing the surface oxygen, slightly improving the CH_4 selectivity. However, adding too much Zr will reduce the catalyst's reactivity because the irregular pore structure increases the Ni particle size, leading to the ability to adsorb OCO* too strongly and reducing the activity of the catalyst. Another property leading to the distinction in product selectivity in the temperature range of 250–––300 °C (Fig. 4b) could be the CO_2 adsorption capacity, relating to the catalysts' CO_2-TPD profiles. While suitable amount of ZrO_2 with moderate basic sites could promote the formation of CH_4 in the low temperatures, the excess loading of ZrO_2 inducing a lower Ni density on the surface could favor the formation of nickel carbonyl, which later convert into CO in the product flow. The slow kinetic nature of the reaction in the low temperature combining with more CO_2 adsorbed on the catalyst's surface than H_2 might take responsibility for the generation of the metallic carbonyl species (Aziz et al., 2015; Wen et al., 2021). Therefore, adding an appropriate amount of Zr can improve the reactivity of the catalysts. Within the scope of this work, the 10Ni4Zr/HA catalyst showed optimal CO_2 conversion. A schematic of CO_2 methanation on ZrO_2-doped nickel nanocatalyst supported on hydroxyapatite from Salmon bone could be represented in Fig. 5.

Reaction mechanism investigations were carried out to determine how methane is generated on the Ni/HA catalyst surface. In recent years, the CO_2 methanation reaction mechanism has been intensively investigated in order to design a more active and selective catalyst for the synthesis of methane (Wai et al., 2020). Pan et al. proposed a reaction mechanism in which formate species is the primary reaction intermediate while carbonates and hydrogen carbonates are formed in CO_2 methanation (Jia et al., 2020). As shown in [steps (1)–(11)], a reaction mechanism for CO_2 methanation over Ni/HA catalyst is postulated on the basis of these previous studies. The H_2 molecule splits into two hydrogen atoms (step 1) on the Ni surface (*). In steps (2)-(5), gaseous CO_2 chemisorbs and reacts with surface hydroxyl (OH*) to form hydrogen-carbonates (HCO_3*). The hydrogen-carbonate species becomes formate (HCOO*) by reacting with H atoms on the surface (step (6)). In step 4, surface H atoms react with surface O atoms to replenish the surface hydroxyl groups. Through additional hydrogenation (steps (7)-(8)), surface formate also transforms into OCH_2OH* species and then into methoxy species (OCH_3*). The OCH_3* species is then hydrogenated (step (9)) to form CH_4. Additionally, methoxy formation is also associated with the presence of Lewis acidic sites (Kim et al., 2019). Since HA catalytic support is utilized in this work for CO_2 methanation, the Ca (II) sites in the HA unit cell structure are Lewis acidic (Yook et al., 2022), indicating that the HA support plays a role in stabilizing methoxy species generation and influencing methane synthesis.

$$H_{2(g)} + 2^* \leftrightarrow 2H^* \quad (1)$$

$$CO_{2(g)} + ^* \leftrightarrow OCO^* \quad (2)$$

$$OCO^* \leftrightarrow CO_{(g)} + O^* \quad (3)$$

$$H^* + O^* \leftrightarrow ^* + OH^* \quad (4)$$

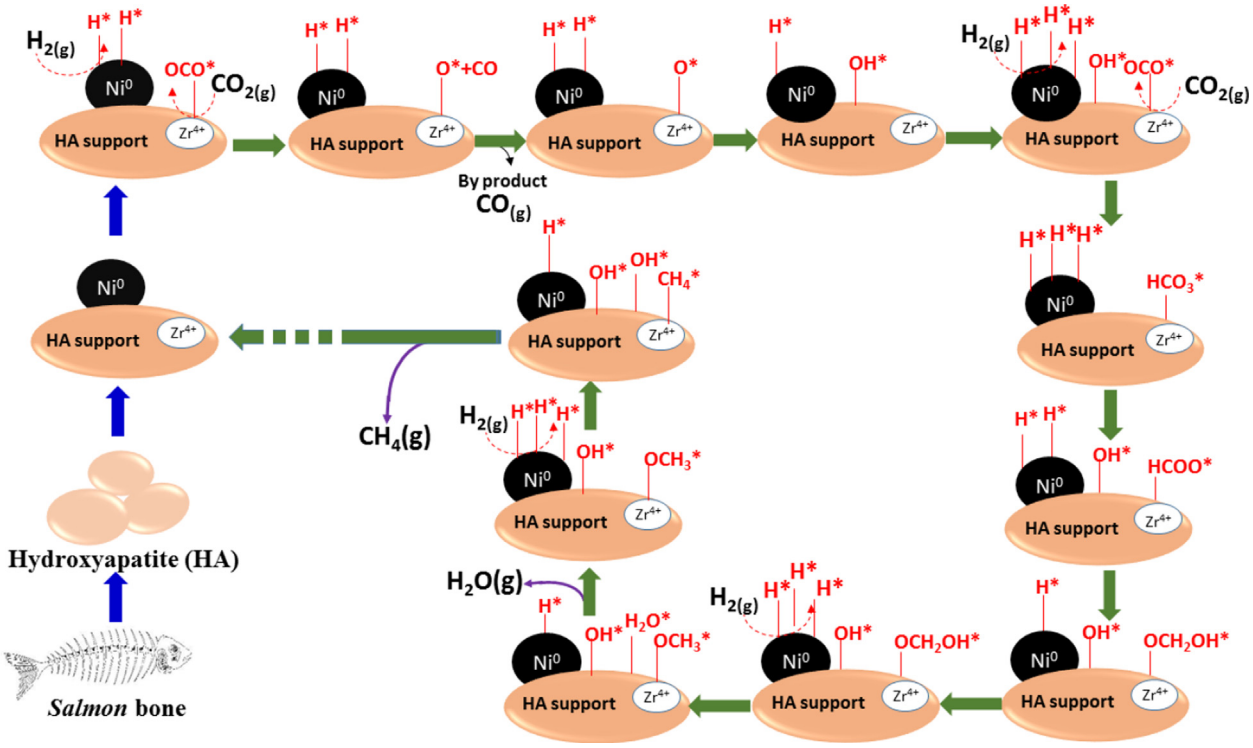

Fig. 5. Schematic representation of CO_2 methanation on NiZr/HA catalyst.

$$OCO^* + OH^* \leftrightarrow HCO_3^* + * \quad (5)$$

$$HCO_3^* + H^* \leftrightarrow HCOO^* + OH^* \quad (6)$$

$$HCOO^* + 2H^* \leftrightarrow OCH_2OH^* + 2^* \quad (7)$$

$$OCH_2OH^* + 2H^* \leftrightarrow OCH_3^* + H_2O^* + * \quad (8)$$

$$OCH_3^* + 2H^* \leftrightarrow CH_4^* + OH^* + * \quad (9)$$

$$CH_4^* \leftrightarrow CH_{4(g)} + * \quad (10)$$

$$H_2O^* \leftrightarrow H_2O_{(g)} + * \quad (11)$$

To provide insight into the suitability of the 10Ni4Zr/HA catalyst, we compare its efficacy to that of various Ni catalysts at the same of reaction temperature and the CO_2: H_2 molar ratio reported in the literature in Table 2. Numerous supports, including SBA-15 (Van et al., 2020); MCM-41 (Yang et al., 2020), CNTs (Romero-Sáez et al., 2018); SiO_2 (Guo and Lu, 2014), Al_2O_3 (Mutz et al., 2017), Pr_2O_3–CeO_4, Sm_2O_3–CeO_4 (Siakavelas et al., 2021), etc have been investigated. In the majority of cases, Ni content higher than 10% wt were supported on them. Despite their relatively modest Ni content, we may conclude that they can compete favourably with these reference formulations. Because HA can self-exchange cations and anions, this can be explained by the characteristic properties of HA. The active metal centers for the reaction can be introduced into the HA structure via ion exchange, and Ca^{2+} ions give the HA surface a weak base nature with the ability to dissociate CO_2 and the OH group to stabilize the active metal, which promotes CO_2 hydrogenation to CH_4. In addition to the active metal's dispersion, the catalyst's fundamental properties and the amount of surface oxygen in the catalyst significantly influence its reactivity. Adding alkaline earth metals (Ca present in HA) can increase the number of active metal sites on the catalyst that influence CO_2 adsorption and activation. Moreover, it is evident that the positive effect of Zr on the activity of the Ni catalyst is more pronounced in our HA-based materials, indicating that our green

Table 2
The comparison of activity of different nickel-based catalysts in CO_2 methanation at the reaction temperature of 350 °C using the CO_2: H_2 molar ratio = 1:4.

Catalyst	Ni, wt%	WGHSV, mL/(g.h)	C_{CO2}, mol%	X_{CO2}, %	Y_{CH4}, %	H, molCO_2/(molNi.h)	Y, molCH_4/(molNi.h)	Refs.
50Ni4Ce/SBA	50	12,000	20	90	99	12.5	12.4	(Van et al., 2020)
10Ni/@Zr(0.01)@MCM-41	10	6,420	10	88.6	96.5	16.5	15.9	(Yang et al., 2020)
5Ni/$Ce_{0.85}Zr_{0.15}O_2$	5	10,000	16	60	100	55.7	55.7	(Iglesias et al., 2019)
5Ni/Zr/CNTs-COI	5	75,000	10	20	70	87.1	60.9	(Romero-Sáez et al., 2018)
10Ni/Ce	10	25,000	10	39.4	100	28.6	28.6	(Siakavelas et al., 2021)
10Ni/Sm-Ce	10	25,000	10	44.9	100	32.6	32.6	(Siakavelas et al., 2021)
10Ni/Pr-Ce	10	25,000	10	54.5	100	39.5	39.5	(Siakavelas et al., 2021)
10Ni/Mg-Ce	10	25,000	10	43.2	100	31.3	31.3	(Siakavelas et al., 2021)
20Ni3Fe/Al_2O_3	20	134,000	10	82	99.0	15.9	15.8	(Mutz et al., 2017)
10Ni4Ca/SiO_2	10	15,000	10	64.9	98.6	28.2	27.9	(Guo and Lu, 2014)
20NiAl-LDH	20	2,400	18.75	75.1	95.0	4.9	4.7	(He et al., 2013)
10Ni4Zr/HA	10	12,000	3	76.6	99.8	8.0	8.0	This work

H – CO_2 conversion efficiency calculated per Ni mole, molCO_2/(molNi.h); Y - CH_4 yield calculated per Ni mole, molCH_4/(molNi.h).

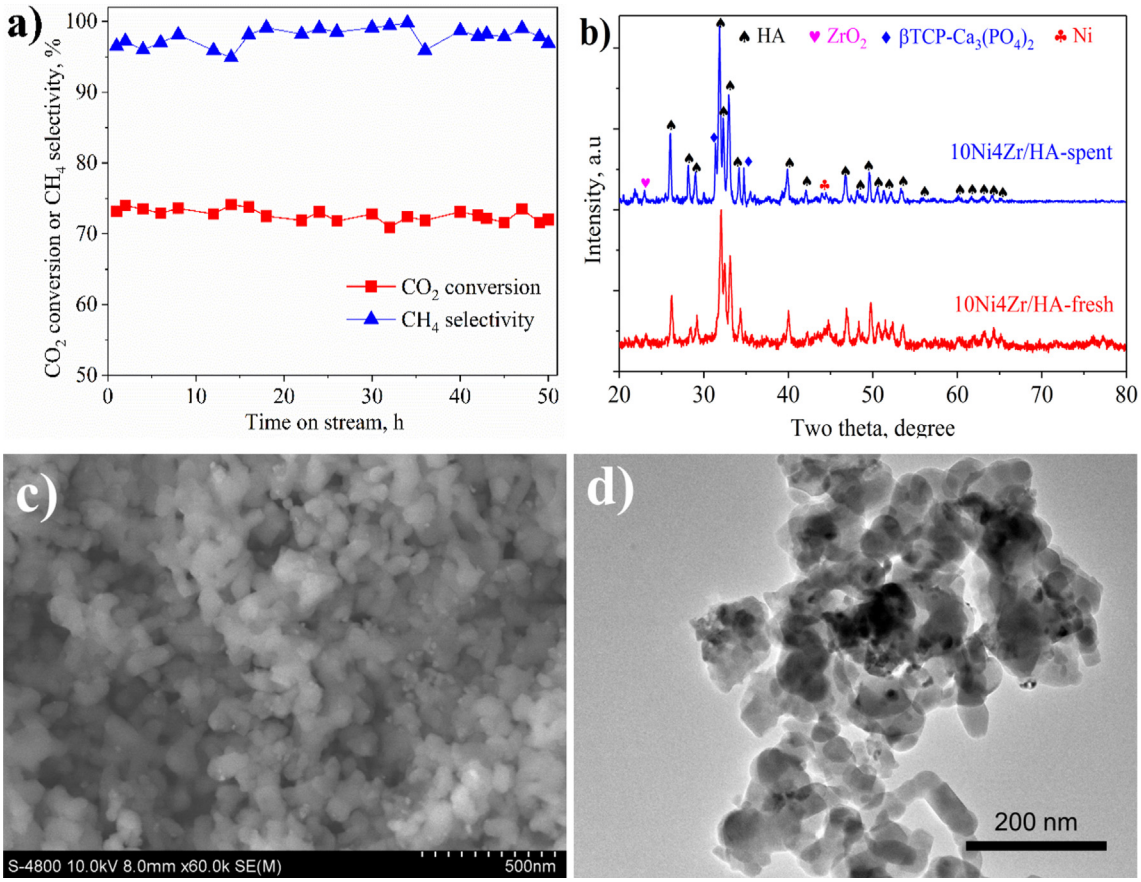

Fig. 6. The activity stability of the best catalyst (10Ni4Zr/HA) in CO_2 methanation at 350 °C during 50 h on stream (a), XRD pattern (d), and SEM (b) and TEM (c) images of spent catalyst.

support is suitable for the CO_2 methanation reaction. It should be emphasized that the enhanced structural, chemical, and catalytic properties of Ni-based catalysts supported on hydroxyapatite-derived Salmon bone waste represent an advantageous alternative to conventional basic catalysts.

3.3. The stability of 10Ni4Zr/HA catalyst

The stability test, performed at 350 ∘C, reveals a robust performance of the optimized 10Ni4Zr/HA catalyst very notable stability during long time on stream (Fig. 6a). After an activation period of 50 h of reaction, reaching a CO_2 conversion close to 76% and a high selectivity towards methane production (>95%). In addition, compared with the characterizations of the initial fresh 10Ni4Zr/HA catalyst (Fig. 2c and 3b), the characterizations of the spent one (Fig. 6b-d) revealed insignificant differences in their properties and the distribution of active phases on the HA surface based on the impregnation technique employed.

4. Conclusion

A simple and environmentally friendly approach was developed for synthesizing Ni/HA and ZrO_2-doped Ni/HA catalysts for CO_2 methanation. Ca^{2+} ions in the HA structure promoted CO_2 adsorption, increasing catalytic activity. Adding the zirconia to the Ni/HA catalyst enhances NiO dispersion on the HA surface, leading to smaller NiO crystals, an increased NiO reduction and CO_2 adsorption capacity, and better catalytic activity. At 400 °C, the 10Ni/HA catalyst-doped 4 wt% ZrO_2 showed outstanding catalytic performance, with a CO_2 conversion of 92.9% and a CH_4 selectivity of almost 100%. As a result, one of the most promising techniques in developing effective catalyst designs toward the development of effective CO_2 hydrogenation to CH_4 fuel on an industrial scale is employing a zirconia-doped Ni/HA catalyst.

CRediT authorship contribution statement

Ngoc Doan Trang Tran: Methodology, Resources, Writing – original draft, Validation, Investigation, Formal analysis. **Thi Ngoc Han Che:** Methodology, Resources, Writing – original draft, Validation, Investigation, Formal analysis. **Thi Thuy Van Nguyen:** Conceptualization, Methodology, Resources, Writing – original draft, Validation, Investigation, Formal analysis. **Ba Long Do:** Methodology, Resources, Writing – original draft, Validation, Investigation, Formal analysis. **Thanh Gia-Thien Ho:** Conceptualization, Methodology, Resources, Writing – original draft, Validation, Investigation, Formal analysis. **Phung Anh Nguyen:** Methodology, Resources, Writing – original draft, Validation, Investigation, Formal analysis. **Thi Thuy Phuong Pham:** Conceptualization, Methodology, Resources, Writing – original draft, Validation, Investigation, Formal analysis. **Nguyen Tri:** Conceptualization, Methodology, Writing – review & editing, Supervision. **Huynh Ky Phuong Ha:** Conceptualization, Methodology, Writing – review & editing, Supervision.

Declaration of Competing Interest

The authors declare that they have no known competing financial interests or personal relationships that could have appeared to influence the work reported in this paper.

Acknowledgments

This study is supported by the Vietnam Academy of Science and Technology under the NCXS02.02/22-23 project.

References

Aziz, M., Jalil, A., Triwahyono, S., Ahmad, A., 2015. CO_2 methanation over heterogeneous catalysts: Recent progress and future prospects. Green Chem. 17, 2647–2663.
Bakar, W.A.W.A., Ali, R., Mohammad, N.S., 2015. The effect of noble metals on catalytic methanation reaction over supported Mn/Ni oxide based catalysts. Arab. J. Chem. 8, 632–643.
Boukha, Z., Yeste, M.P., Cauqui, M.Á., Gonzalez-Velasco, J.R., 2019. Influence of Ca/P ratio on the catalytic performance of Ni/hydroxyapatite samples in dry reforming of methane. Appl. Catal. A: Gen. 580, 34–45.
Boukha, Z., Yeste, M.P., Cauqui, M.Á., González-Velasco, J.R., 2019. Influence of Ca/P ratio on the catalytic performance of Ni/hydroxyapatite samples in dry reforming of methane. Appl. Catal. A: Gen. 580, 34–45.
Boukha, Z., Bermejo-López, A., Pereda-Ayo, B., González-Marcos, J.A., González-Velasco, J.R., 2022. Study on the promotional effect of lanthana addition on the performance of hydroxyapatite-supported Ni catalysts for the CO_2 methanation reaction. Appl. Catal. B: Environ. 314, 121500.
Cai, M., Wen, J., Chu, W., Cheng, X., Li, Z., 2011. Methanation of carbon dioxide on Ni/ZrO_2-Al_2O_3 catalysts: Effects of ZrO_2 promoter and preparation method of novel ZrO_2-Al_2O_3 carrier. J. Nat. Gas Chem. 20, 318–324.
Chong, C.C., Teh, L.P., Setiabudi, H.D., 2019. Syngas production via CO2 reforming of CH4 over Ni-based SBA-15: Promotional effect of promoters (Ce, Mg, and Zr). Mater. Today Energy 12, 408–417.
Daza, C.E., Kiennemann, A., Moreno, S., Molina, R., 2009. Dry reforming of methane using Ni–Ce catalysts supported on a modified mineral clay. Appl. Catal. A: Gen. 364, 65–74.
Diallo-Garcia, S., Osman, M.B., Krafft, J.-M., Casale, S., Thomas, C., Kubo, J., Costentin, G., 2014. Identification of surface basic sites and acid–base pairs of hydroxyapatite. J. Phys. Chem. C 118, 12744–12757.
El Shafei, G.M., Philip, C.A., Moussa, N.A., 2004. Fractal analysis of hydroxyapatite from nitrogen isotherms. J. Colloid Interface Sci. 277, 410–416.
Guo, M., Lu, G., 2014. The difference of roles of alkaline-earth metal oxides on silica-supported nickel catalysts for CO_2 methanation. RSC Adv. 4, 58171–58177.
He, S., Li, C., Chen, H., Su, D., Zhang, B., Cao, X., Wang, B., Wei, M., Evans, D.G., Duan, X., 2013. A surface defect-promoted Ni nanocatalyst with simultaneously enhanced activity and stability. Chem. Mater. 25, 1040–1046.
Iglesias, I., Quindimil, A., Mariño, F., De-La-Torre, U., González-Velasco, J.R., 2019. Zr promotion effect in CO_2 methanation over ceria supported nickel catalysts. Int. J. Hydrog. Energy 44, 1710–1719.
Jia, X., Sun, K., Wang, J., Shen, C., Liu, C.-J., 2020. Selective hydrogenation of CO_2 to methanol over Ni/In_2O_3 catalyst. J. Energy Chem. 50, 409–415.
Jiang, W., Loh, H., Low, B.Q.L., Zhu, H., Low, J., Heng, J.Z.X., Tang, K.Y., Li, Z., Loh, X.J., Ye, E., 2022. Role of oxygen vacancy in metal oxides for photocatalytic CO_2 reduction. Appl. Catal. B: Environ. 122079
Kim, J., Sarma, B.B., Andrés, E., Pfänder, N., Concepción, P., Prieto, G., 2019. Surface lewis acidity of periphery oxide species as a general kinetic descriptor for CO_2 hydrogenation to methanol on supported copper nanoparticles. ACS Catal. 9, 10409–10417.
Komatsu, T., Furukawa, S., 2015. Intermetallic compound nanoparticles dispersed on the surface of oxide support as active and selective catalysts. Mater. Trans. 56, 460–467.
Kuznecova, I., Gusca, J., 2017. Property based ranking of CO and CO_2 methanation catalysts. Energy Procedia 128, 255–260.
Le, H., Chen, K., Wang, C., 2012. Effect of pH and temperature on the morphology and phases of co-precipitated hydroxyapatite. J. Solgel Sci. Technol. 61, 592–599.
Lee, W.J., Li, C., Prajitno, H., Yoo, J., Patel, J., Yang, Y., Lim, S., 2021. Recent trend in thermal catalytic low temperature CO_2 methanation: A critical review. Catal. Today 368, 2–19.
Li, K., Chen, J.G., 2019. CO_2 hydrogenation to methanol over ZrO_2-containing catalysts: insights into ZrO_2 induced synergy. ACS Catal. 9, 7840–7861.
Li, S., Falconer, J.L., Noble, R.D., 2006. Improved SAPO-34 membranes for CO2/CH4 separations. Adv. Mater. 18, 2601–2603.
Li, Y., Zhang, C., Zhang, T., Ma, P., Yu, Y., Zhang, Z., Wang, G.G., 2023. Experimental and DFT study on single atom solution for carbon dioxide methanation. Fuel 351, 128911.
Mebrahtu, C., Krebs, F., Abate, S., Perathoner, S., Centi, G., Palkovits, R., 2019. CO_2 methanation: principles and challenges. In: Studies in Surface Science and Catalysis. Elsevier, pp. 85–103.
Mihet, M., Lazar, M.D., 2018. Methanation of CO_2 on Ni/γ-Al_2O_3: influence of Pt, Pd or Rh promotion. Catal. Today 306, 294–299.
Muiruri, J.K., Ye, E., Zhu, Q., Loh, X.J., Li, Z., 2022. Recent advance in nanostructured materials innovation towards photocatalytic CO_2 reduction. Appl. Catal. A: Gen. 648, 118927.
Mutz, B., Belimov, M., Wang, W., Sprenger, P., Serrer, M.-A., Wang, D., Pfeifer, P., Kleist, W., Grunwaldt, J.-D., 2017. Potential of an alumina-supported Ni_3Fe catalyst in the methanation of CO_2: Impact of alloy formation on activity and stability. ACS Catal. 7, 6802–6814.
Namvar, F., Salavati-Niasari, M., Mahdi, M.A., Meshkani, F., 2023. Multidisciplinary green approaches (ultrasonic, co-precipitation, hydrothermal, and microwave) for fabrication and characterization of Erbium-promoted Ni-Al2O3 catalyst for CO2 methanation. Arab. J. Chem. 16, 104494.
Pal, A., Hadagalli, K., Bhat, P., Goel, V., Mandal, S., 2020. Hydroxyapatite - A promising sunscreen filter. J. Aust. Ceram. Soc. 56, 345–351.
Pan, Q., Peng, J., Sun, T., Wang, S., Wang, S., 2014. Insight into the reaction route of CO_2 methanation: Promotion effect of medium basic sites. Catal. Commun. 45, 74–78.
Roh, H.-S., Potdar, H., Jun, K.-W., 2004. Carbon dioxide reforming of methane over co-precipitated Ni-CeO_2, Ni-ZrO_2 and Ni-Ce-ZrO_2 catalysts. Catal. Today 93, 39–44.
Romero-Sáez, M., Dongil, A., Benito, N., Espinoza-González, R., Escalona, N., Gracia, F., 2018. CO_2 methanation over nickel-ZrO_2 catalyst supported on carbon nanotubes: A comparison between two impregnation strategies. Appl. Catal. B: Environ. 237, 817–825.
Siakavelas, G.I., Charisiou, N.D., AlKhoori, S., AlKhoori, A.A., Sebastian, V., Hinder, S.J., Baker, M.A., Yentekakis, I., Polychronopoulou, K., Goula, M.A., 2021. Highly selective and stable nickel catalysts supported on ceria promoted with Sm_2O_3, Pr_2O_3 and MgO for the CO_2 methanation reaction. Appl. Catal. B: Environ. 282, 119562.
Soni, D., Singh, J., Kaurav, N., Tripathi, J., Sharma, A., 2022. Synthesis and characterization of zirconia nanocrystalline powder by thermal treatment method. Mater. Today:. Proc. 54, 908–911.
Srihasam, S., Thyagarajan, K., Korivi, M., Lebaka, V.R., Mallem, S.P.R., 2020. Phytogenic generation of NiO nanoparticles using Stevia leaf extract and evaluation of their in-vitro antioxidant and antimicrobial properties. Biomolecules 10, 89.
Su, X., Xu, J., Liang, B., Duan, H., Hou, B., Huang, Y., 2016. Catalytic carbon dioxide hydrogenation to methane: A review of recent studies. J. Energy Chem. 25, 553–565.
Tamai, M., Isama, K., Nakaoka, R., 2007. Synthesis of a novel beta-tricalcium phosphate/hydroxyapatite biphasic calcium phosphate containing niobium ions and evaluation of its osteogenic properties. J. Artif. Organs 10, 22–28.
Tri, N., Trang, T., Trinh, N., Tung, L.T., Van, N., Anh, N.P., Tan, N.D., No, N., Ha, H., 2020. Hydrothermal and calcination regimes and characteristics of nanohydroxyapatite synthesized from Salmon bones. J. Biochem. Technol. 11, 82–87.
Van, N.T., Loc, L.C., Anh, N.P., Cuong, H.T., Tri, N., 2020. Positive effects of CeO_2 promoter and co-reactant/CO on methanation of CO_2-rich gas over Ni/SBA-15 catalyst. Mater. Trans. 61, 1332–1338.
Wai, M.H., Ashok, J., Dewangan, N., Das, S., Xi, S., Borgna, A., Kawi, S., 2020. Influence of surface formate species on methane selectivity for carbon dioxide methanation over nickel hydroxyapatite catalyst. ChemCatChem 12, 6410–6419.
Wai, S., Ota, Y., Nishioka, K., 2021. Performance analysis of sabatier reaction on direct hydrogen inlet rates based on solar-to-gas conversion system. Int. J. Hydrog. Energy 46, 26801–26808.
Wang, X., Liu, Y., Zhu, L., Li, Y., Wang, K., Qiu, K., Tippayawong, N., Aggarangsi, P., Reubroycharoen, P., Wang, S., 2019. Biomass derived N-doped biochar as efficient catalyst supports for CO_2 methanation. J. CO_2 Util. 34, 733–741.
Wen, X., Xu, L., Chen, M., Shi, Y., Lv, C., Cui, Y., Wu, X., Cheng, G., Wu, C.-E., Miao, Z., 2021. Exploring the influence of nickel precursors on constructing efficient Ni-based CO_2 methanation catalysts assisted with in-situ technologies. Appl. Catal. B: Environ. 297, 120486.
Yang, M., Lingjun, Z., Xiaonan, Z., Prasert, R., Shurong, W., 2020. CO_2 methanation over nickel-based catalysts supported on MCM-41 with in situ doping of zirconium. J. CO_2 Util. 42, 101304.
Ye, D., Liu, L., Peng, Q., Qiu, J., Gong, H., Zhong, A., Liu, S., 2023. Effect of controlling thiophene rings on DA polymer photocatalysts accessed via direct arylation for hydrogen production. Molecules 28, 4507.
Yook, H., Hwang, J., Yeo, W., Bang, J., Kim, J., Kim, T.Y., Choi, J.S., Han, J.W., 2022. Design strategies for hydroxyapatite-based materials to enhance their catalytic performance and applicability. Adv. Mater. 2204938.
Zhao, J., Patwary, A.K., Qayyum, A., Alharthi, M., Bashir, F., Mohsin, M., Hanif, I., Abbas, Q., 2022. The determinants of renewable energy sources for the fueling of green and sustainable economy. Energy 238, 122029.